Article

A Polymorphing Wing Capable of Span Extension and Variable Pitch

Muhammed S. Parancheerivilakkathil [1], Zawar Haider [1], Rafic M. Ajaj [1,*] and Mohammadreza Amoozgar [2]

[1] Department of Aerospace Engineering, Khalifa University of Science and Technology, Abu Dhabi 127788, United Arab Emirates; muhammed.sadique@ku.ac.ae (M.S.P.); 100057743@ku.ac.ae (Z.H.)
[2] Department of Mechanical, Materials and Manufacturing Engineering, University of Nottingham, Nottingham NG7 2RD, UK; m.amoozgar@nottingham.ac.uk
* Correspondence: rafic.ajaj@ku.ac.ae; Tel.: +971-(0)-2-3124238

Abstract: This paper presents the development of a novel polymorphing wing capable of Active Span morphing And Passive Pitching (ASAPP) for small UAVs. The span of an ASAPP wing can be actively extended by up to 25% to enhance aerodynamic efficiency, whilst its pitch near the wingtip can be passively adjusted to alleviate gust loads. To integrate these two morphing mechanisms into one single wing design, each side of the wing is split into two segments (e.g., inboard and outboard segments). The inboard segment is used for span extension whilst the outboard segment is used for passive pitch. The inboard segment consists of a main spar that can translate in the spanwise direction. Flexible skin is used to cover the inboard segment and maintain its aerodynamic shape. The skin transfers the aerodynamic loads to the main spar through a number of ribs that can slide on the main spar through linear plain bearings. A linear actuator located within the fuselage is used for span morphing. The inboard and outboard segments are connected by an overlapping spar surrounded by a torsional spring. The overlapping spar is located ahead of the aerodynamic center of the outboard segment to facilitate passive pitch. The aero-structural design, analysis, and sizing of the ASAPP wing are detailed here. The study shows that the ASAPP wing can be superior to the baseline wing (without morphing) in terms of aerodynamic efficiency, especially when the deformation of the flexible skin is minimal. Moreover, the passive pitching near the wingtip can reduce the root loads significantly, minimizing the weight penalty usually associated with morphing.

Keywords: span morphing; variable pitch; flexible skin; UAVs

1. Introduction

The Advisory Council for Aeronautics Research in Europe (ACARE) FlightPath 2050 report urged a 75% reduction in CO_2 emissions per passenger kilometer, a 90% reduction in NOx emissions, and a 65% reduction in the perceived noise emission of flying aircraft [1]. Morphing aircraft is a promising technology that can help in mitigating the adverse effects of flight and meet the FlightPath 2050 goals. In addition, morphing wings can increase maximum lift, reduce drag [2,3] and vibrations, improve flight performance within a certain airspeed range [4], and enhance aeroelastic performance [5,6] and aircraft maneuverability [7,8]. By definition, a morphing aircraft continuously adjusts its geometry to enhance flight performance, control authority, and multi-mission capability. In the last decade, extensive reviews of morphing technologies, and methods and tools used for modeling and analyzing morphing aircraft have been presented [9]. It is apparent from the literature that most of the morphing technologies have focused on wings with single morphing degrees of freedom. However, it is anticipated that the full potential of morphing technologies can be further achieved when multiple morphing degrees of freedom are combined (polymorphing). This paper develops a polymorphing wing capable of active span extension and passive pitch/twist variation. In what follows, several representative examples of span morphing wings and twist/pitch morphing concepts are highlighted.

1.1. Span Morphing Literature

Aircraft with high aspect ratio wings have some advantages, such as increased fuel efficiency and extended range, and some disadvantages, such as relatively low cruise speeds and lack of agility/maneuverability. Aircraft with low aspect ratio wings, on the other hand, have high margins of agility and can fly faster but show poor aerodynamic efficiency [10]. Integrating the benefits of both designs, an aircraft with a span morphing wing can effectively perform at various flight missions, making this emerging technology attractive for multi-mission UAVs. The first aircraft with a span morphing wing, the MAK-10, which flew in 1931, was developed by Ivan Makhonine. The MAK-10 was capable of achieving span extensions up to 62% using a pneumatically powered telescopic mechanism [11]. Figure 1 shows a number of aircraft with span morphing wings that have been built and flown in past [5].
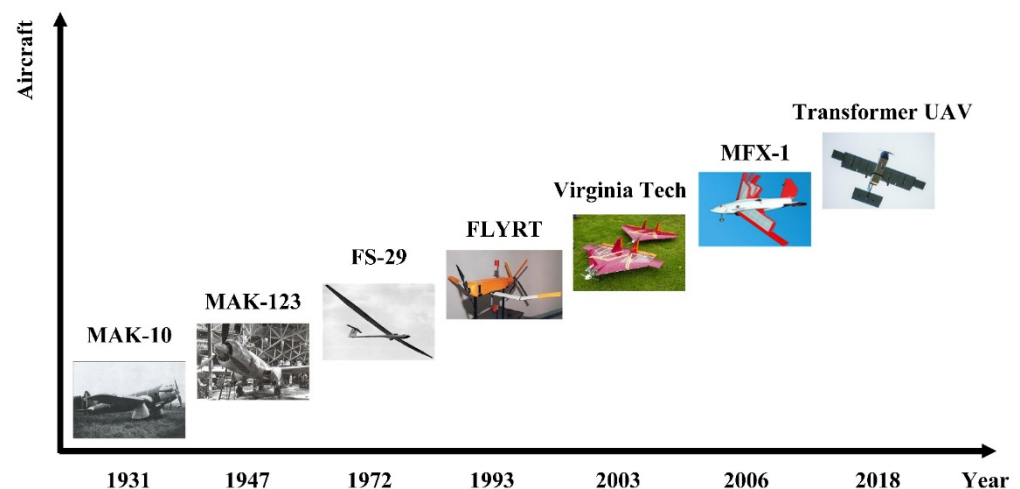

Figure 1. Aircraft that flew with span morphing wings. Reprinted/adapted with permission from Ref. [5]. 2020, Elsevier Ltd.

Most of the span morphing concepts are based on the telescopic mechanism. For instance, the Transformer UAV [12] used a rack and pinion mechanism driven by stepper motors to achieve symmetric and asymmetric span extensions of up to 50%. Wind-tunnel and flight tests were conducted to confirm the enhanced aerodynamic efficiency of the proposed concept.

Another example of telescopic span morphing wings was developed by Blondeau and Pines [13]. It was a three-segmented telescopic wing, in which hollow fiberglass was used to preserve the airfoil geometry and ensure the deployment of the telescopic wing. To reduce the wing weight, the rigid wing spars were replaced by inflatable telescopic spars, which could support the aerodynamic loads. The spars consisted of concentric circular tubes of decreasing diameter and increasing length, ended by pistons. The extension of the spar was achieved by air pressure input at the root, while retraction was obtained by reverse pressure at different locations on the spar. The benefits of the proposed concept were confirmed through a series of wind-tunnel tests.

On the other hand, a number of compliant span morphing concepts have also been proposed. For example, Ajaj et al. [14] introduced a concept called Zigzag wingbox, which consisted of morphing and rigid parts, and was able to increase the wingspan by 44% (22% extension and 22% retraction). The rigid part accommodates the fuel tank and transfers the aerodynamic loads from the morphing part to the fuselage. The morphing part is divided into different segments and each one consists of two beams hinged together, which act as a spar. Varying the angle between the two beams allows for the change in span. The study suggested the use of a Zero-Poisson's ratio cellular core reinforced elastomeric matrix composite (EMC) skin to restrict bending deformations and maintain the aerodynamic shape of the airfoil. Moreover, Ajaj et al. [15] introduced a novel gear-driven autonomous

twin-spar (GNATSpar) morphing concept for a mini-UAV that can achieve span extension up to 20%. A rack and pinion mechanism was used to achieve symmetric span morphing. The GNATSpar was connected to two racks, which moved upon actuation, to a number of ribs that were covered by elastomeric skin to allow span variations. In contrast to other telescopic span morphing wings, the GNATSpar used the space available on the opposite side of the wing to accommodate the rack during the retracted position. Wind-tunnel testing showed that the aerodynamic efficiency of the UAV increased with span extension.

Vocke III et al. [16] utilized a zero-Poisson's ratio airfoil-like compliant core for continuous span morphing, which consisted of a series of 'rows' or 'ribs' of constant length that were connected by 'V-shaped' bending elements. The honeycomb/core was covered by fiber-reinforced EMC skin with a nearly zero in-plane Poisson ratio [17]. Carbon fibers were aligned and sandwiched between two Rhodorsil elastomer sheets to shape the EMC skin. Wind-tunnel tests were conducted to confirm the out-of-plane stiffness of the manufactured wing segment. Moreover, Woods and Friswell [18,19] developed an Adaptive Aspect Ratio (AdAR) wing, which coupled a compliant skin with a mechanism-based internal structure to enable a significant change in the wingspan and aspect ratio. The AdAR wing consisted of an EMC skin, a telescopic rectangular box spar, sliding ribs, and a strap drive system. The actuation system connects the inner moving portion of the telescopic spar to the outer fixed portion by a high strength strap, which facilitates the span morphing using the tension in the strap by moving it around redirection pulleys. Simulations were carried out to optimize the skin and study the design parameters affecting it. The optimization study provided a good insight into the mechanics of this highly coupled design problem. Recently, Bishay et al. [20] introduced a new design for the core of a span-morphing UAV capable of 50% continuous span morphing. The wing comprised multiple partitions built with three main components: a zero Poisson's ratio honeycomb substructure, telescoping carbon fiber spars, and a linear actuator. The zero Poisson's ratio honeycomb substructure was assembled using flexible chevrons and internal ribs. The ribs and chevrons were 3D printed separately from different materials. The wing design allowed for maintaining the airfoil shape and cross-sectional area due to its spanwise compliance and transverse rigidity. The telescoping carbon fiber spars allowed for morphing while providing structural support throughout the wing. Finite element simulations were carried out to estimate the actuation force required for span extension and to investigate the structural rigidity of the spars and honeycomb substructure. In addition, the manufactured wing segment was tested for estimating the actuation force required. Suggested future works included optimization studies using stretchable skin, wind tunnel tests, and reliability and failure analyses.

In contrast to both telescopic and compliant span morphing concepts, Geva et al. [21] used a folding mechanism for a polymorphing aircraft capable of span extension and camber changes. The wing consisted of two segments, in which the outbound segment can be mechanically folded by means of a hinge and tucked underneath the inbound segment. This mechanism facilitated the span morphing, while the resulting airfoil of the folded plane, which consisted of the inbound airfoil and the inverse outbound airfoil, contributed to camber changes. Firstly, an analysis was performed to study the additional endurance gained by the morphing capabilities compared to standard aircraft. A suggested folding algorithm was then outlined. Finally, the airfoil selection process was detailed, followed by the wind-tunnel test phase. The study showed that the morphing concept, in theory, improved endurance by up to 50% compared to the standard counterparts. The wind-tunnel tests on the wing model showed that the ClarkY 9% airfoil had a superior lift to drag ratio compared to other airfoils.

1.2. Twist/Pitch Morphing Literature

Varying the twist distribution can be used to improve control authority, flight performance, and load alleviation. Twist morphing is considered as the oldest form of morphing as it has been adopted since the earliest days of heavier-than-air aviation.

A number of studies utilized twist morphing to improve aerodynamic performance. For example, Vos et al. [22] utilized a warp-controlled concept for the active twisting of a wing. The twist was achieved by warping displacement of the upper and lower wing surfaces made of CFRP, which had a split at the trailing edge to make an open section airfoil. This was achieved by an internal screw mechanism. The study proved both numerically and experimentally (wind-tunnel tests) that the proposed concept could maximize the lift-to-drag during various flight conditions.

In addition, Rodrigue et al. [23] proposed a novel active twist-morphing concept and studied the effect of twisting on the aerodynamic performance of a UAV wing. The wing consisted of an inner fixed segment and an outer morphing segment, which was actuated to obtain tip twisting. The morphing segment had a polylactic acid (PLA) structure, polydimethylsiloxane (PDMS) matrix, and shape memory alloy (SMA) wires. The PLA structure and SMA wires were embedded in the PDMS. The SMA wires crossed the PDMS matrix in opposite directions and were positioned at opposite eccentricities [24]. This allowed for a smooth actuation of PLA structure using SMA wires. The actuation test showed that the wing was capable of achieving a twist angle of 6.25°. In addition, wind-tunnel tests were conducted to confirm the aerodynamic performance improvement of this concept. Schlup et al. [25] presented a morphing UAV called MetaMorph 2 (XM-2) capable of wing twist-morphing and camber morphing of the tail-stabilizer that could perform all required maneuvers without any discrete control surfaces. The main wing, capable of $\pm15°$ range of twisting motion, had three segments. The root and tip segments were laminated using composite skin sections and the middle twisting section was made of polyurethane foam covered by a smooth flexible skin. The wing structure was designed using balsa wood. Twisting in the morphing middle segment was achieved by means of a motor gearbox mechanism that was accommodated inside the fuselage. The tail stabilizer consisted of a rigid leading-edge section and a camber morphing corrugated trailing edge section, which actuated using a servomotor and Carbitex CX6 ribbons. Finite element analysis was carried out to investigate the deflection in the skin, which showed a maximum of 0.4 mm deflection. CFD simulations also showed that the continuous wing surface had improved the overall aircraft efficiency. Mechanical testing was conducted on different components to confirm the structural integrity.

Rea et al. [26] presented the preliminary design of a full-scale composite multifunctional and twistable trailing edge, retrofitting the outboard morphing fowler flap of a regional turboprop aircraft. The flap tab/trailing edge device could activate two modes of functionalities when the fowler flap was stowed in the wing during different flight conditions: rigid downward/upward deflections of the Fowler flap tip segment (mode A) and continuous span-wise twist with a maximum differential twist-angle of 10° between the tip and root sections of the flap (up to $\pm5°$ at the root and tip sections respectively) (mode B). The torsional deformation of the flap tab for continuous span-wise twist was achieved using distributed actuators (brushless motors). The study showed that the proposed concept was a promising one to balance the conflicting requirements between load-carrying capability and shape adaptability. An increment of 3.52% in weight of the outboard flap tip segment was produced while retrofitting such a device on a regional aircraft. Finally, high-fidelity aerodynamic analysis using the ONERA elsA code [27] showed that the wing retrofitted with this device improved the airplane aerodynamic efficiency during high-speed climb conditions. In addition, Bishay and Aguilar [28] conducted a parametric study of a composite skin for a twist morphing wing. The skin consisted of periodic laminated composite sections called "Twiskins", integrated with an elastomeric outer skin, which facilitated localized twisting deformation between the Twiskins. The study considered the number of plies in the composite Twiskins, fiber orientation angle of plies, number of elastomeric sections, the torsional rigidity of the elastomer, and the width ratio as design parameters. The effects of these parameters on torsional compliance and out-of-plane stiffness were studied with the aid of CFD and FEA analyses. The study showed that the maximum strain in the skin at the most compliant configuration was observed to be 9.97% (<10%). The out-of-plane

stiffness was increased by a factor of 17.5 by changing the fiber orientation angle from 90° to 0°. In addition, the stiffness was significantly increased by adding one extra ply.

On the other hand, some studies utilized twist morphing for load alleviation purposes. For example, Guo et al. [29] studied the influence of a passive twist wingtip (PTWT) for gust and load alleviation on a 200-seater baseline aircraft. Dynamic response analysis to discrete (one-cosine) gusts was performed. The analysis results showed that the PTWT reduced the gust-induced wingtip deflection by 21% and the wing root bending moment by 14% in the most critical flight phases. The PTWT reduced the rolling control effectiveness by reducing the rolling moment by up to 20.5%.

As an extension of the author's previous work [30], this paper presents the design, modeling, manufacturing, and mechanical testing of a polymorphing wing capable of Active Span morphing And Passive Pitching (ASAPP) suitable for small UAVs with low altitude mapping and surveying missions. The wing consists of two segments for integrating two morphing degrees of freedom independently on a single wing. The span extension in the inboard segment is facilitated using a linear actuator, while the outboard segment pitches/rotate around an overlapping spar passively to reduce the root loads. A torsional spring that connects two segments is used to limit the pitch. Aerodynamic analysis using XFLR5 is carried out to find the possible pitch angles and angle of attacks during the cruise for different span extensions and to determine the maximum span extension. Aeroelastic analysis is carried out to size the torsional spring and structural sizing and analysis are carried out using Femap with NX Nastran. Moreover, aerodynamic analysis is conducted to evaluate the effect of the deformed elastomeric skin on the aerodynamic efficiency for different span extensions. Finally, the ASAPP wing is manufactured and mechanically tested.

2. The Polymorphing Concept

2.1. The ASAPP Wing

A small UAV with a rectangular, un-swept, and un-tapered wing is considered as the basis for this study. The baseline wing of the UAV has a chord length of 0.25 m and a span of 1.25 m. It utilizes a NACA 0012 airfoil, and it has a maximum takeoff weight of 4 kg and cruises at 20 m/s. The baseline wing (non-morphing) is replaced with the ASAPP wing. It should be noted that the ASAPP wing (before morphing) has the same dimensions as the baseline wing. To integrate active span morphing and passive pitching into a single wing, each side of the wing is split into two main segments: an inboard segment for span extension and an outboard segment for variable pitch, as shown in Figure 2.

The inboard segment consists of a main spar that can translate in the spanwise direction. The segment is covered by flexible elastomeric skin (latex) to maintain the aerodynamic profile of the wing. To minimize the out-of-plane deformation of the skin, three ribs along with two riblets are used to support the skin (as shown in Figure 3). Before morphing, the span of the inboard segment is 312.5 mm, whilst that of the outboard segment is 212.5 mm, as shown in Figure 2. Keeping a larger segment for inboard span extension induces less strain in the latex skin at maximum extension compared with when using a smaller segment. The root rib is fixed to the walls of the fuselage whilst the middle rib and the riblets can slide on the main spar to allow the skin to stretch uniformly using linear plain bearings. The tip rib (of the inboard segment) is fixed to the end of the main spar, and the flexible skin is attached to it. As the spar translates in the spanwise direction, the tip rib moves with it, causing the skin to stretch. The main spars are made from Aluminum and are connected to the fuselage using Aluminum rails. They are located at 30% of the chord and they have a hollow square cross-section to prevent sliding ribs from rotating around them (Figure 3). Rails are used to transfer the loads from the spars to the fuselage; in addition, they prevent chordwise movement of the main spars. Span extension actuation is achieved by a linear actuator placed in the fuselage along its longitudinal direction. The actuator is connected to the main spars using levers, hinges, and a hinge block, as shown in Figures 2 and 3. It should be noted that only one linear actuator is required because ASAPP is capable only of symmetric span extension.
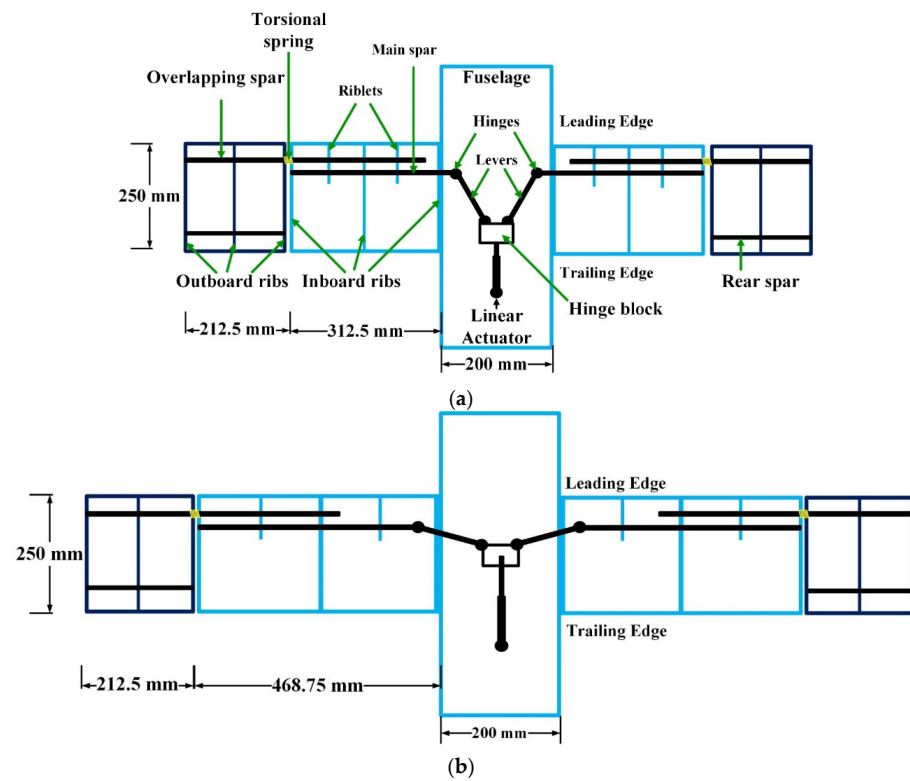
Figure 2. Schematic (top-view) of the ASAPP wing concept: (**a**) Before span extension. (**b**) After span extension.
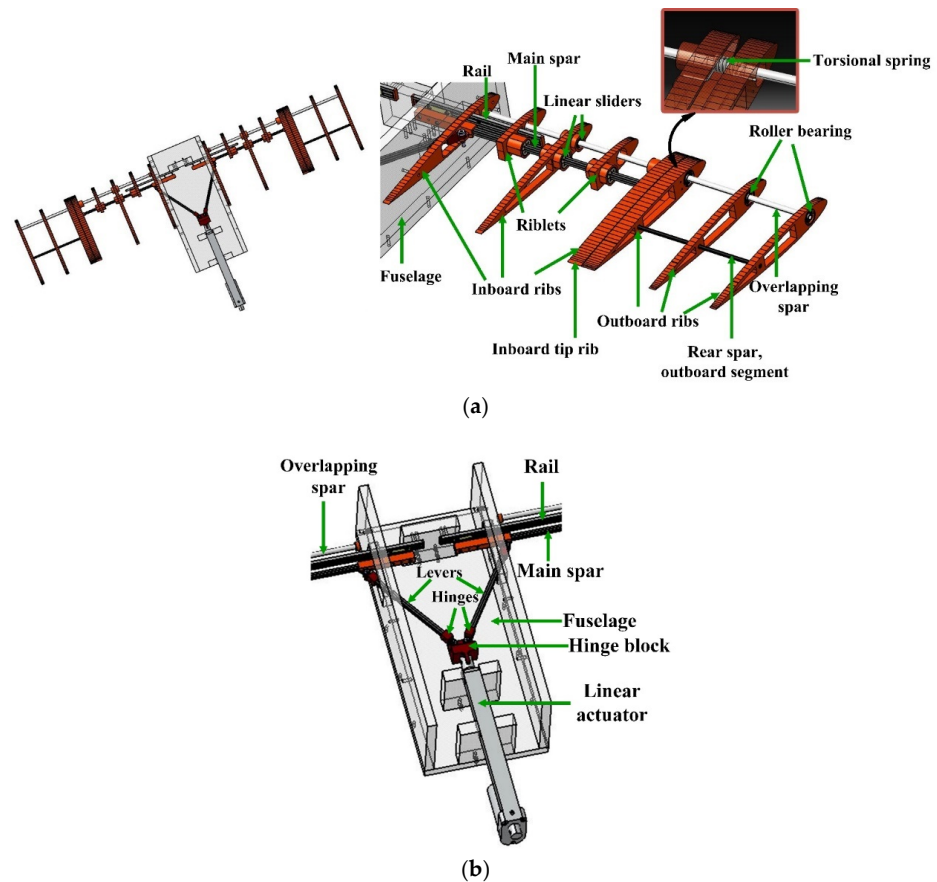

Figure 3. Detailed cad model of the ASAPP wing: (**a**) ASAPP wing. (**b**) Actuation mechanism.

On the other hand, the outboard segment is connected to the inboard one using an overlapping hollow circular spar made from Aluminum and located at 15% of the chord (as shown in Figure 2). The overlapping spar is the main loading bearing structural component in the outboard segment. It should be noted that the portion of the overlapping spar, located in the inboard segment, is always attached to two ribs (tip and middle) of the inboard segment, regardless of the span extension to maximize load transfer between the two segments, as shown in Figure 3. The overlapping spar translates relative to these two ribs using linear slide bearings with a circular cross-section.

The outboard segment is covered by MonoKote lightweight plastic wrap film to maintain the aerodynamic profile. The skin is supported by three ribs (in each outboard segment) to minimize out-of-plane deformations and transfer the aerodynamic loads to the overlapping spar. It should be noted that the three ribs (and the MonoKote skin) can rotate/pitch around the overlapping spar using ball bearings. A CFRP solid circular rear spar at 60% chord is attached to the outboard segment to ensure that the three ribs rotate together around the overlapping spar. Pitch variations occur passively whenever the lift is generated by the outboard segment, mainly because the overlapping spar (at 15% chord) is ahead of the aerodynamic center (around 25% of the chord) of the segment. To limit the amount of pitch, a torsional spring surrounds the overlapping spar and connects the inboard and outboard segments together (Figure 3a).

2.2. Modes of Operation

The ASAPP wing facilitates multi-mission capability by allowing a short wingspan configuration for missions that require agility and maneuverability and a long wingspan configuration for missions that require extended range/endurance. It should be noted that, as the wingspan extends to enhance the aerodynamic efficiency, the outboard segment pitches down, off-loading the wingtip and shifting the lift distribution inboard, further enhancing aerodynamic efficiency and reducing root loads. Regardless of the mission and the UAV configuration, in case the UAV faces turbulence and/or gust, the outboard segment passively pitches down, alleviating the root loads. Under normal flight conditions, the torsional spring limits the nose-down pitch of the outboard segment with respect to the inboard segment [30].

3. Aerodynamic Analysis

The aim of this section is to determine the optimal span extension and pitch angle to maximize the aerodynamic efficiency by reducing the drag during the 1-g flight. XFLR5, an aerodynamic solver that uses XFOIL as its computation kernel with 3D wing capability, is used for aerodynamic predictions for the complete wing (inboard and outboard section) [15]. It incorporates the vortex lattice method (VLM). The profile drag is determined by interpolating the XFOIL drag polar with the angle of attack (α) and Reynolds number [31]. The baseline (non-morphing) wing, cruising at 20 m/s with a 6.88° angle of attack (coefficient of lift (C_L) is 0.5) is modeled in XFLR5. Then, various configurations of the ASAPP wing are analyzed (corresponding to 0%, 25%, 37.5%, and 50% span extensions and 2.5°, 5°, 7.5°, and 10° nose-down pitch angles).

3.1. Aerodynamic Mesh Convergence

To ensure the accuracy and robustness of the aerodynamic results from XFLR5, a mesh convergence study is carried out. The analysis is performed for both 2D airfoil and 3D wing. The analysis on the 2D airfoil is to determine the required number of panel nodes, while the study on the 3D baseline wing (non-morphing) is to determine the required mesh density (number of mesh elements per unit area). Different angles of attack are considered at a velocity of 20 m/s. The study shows that 150 panel nodes are sufficient for 2D analysis and for the 3D baseline wing; mesh convergence occurs when the mesh density exceeds 12,800 elements/m^2 regardless of α. Convergence is achieved once the change in the lift to drag ratio is less than 0.5%.

3.2. Aerodynamic Results

To ensure consistency when comparing the aerodynamic results of the baseline wing and the ASAPP wing (at various configurations), all coefficients are normalized using the baseline wing area, span, and mean aerodynamic chord. The aerodynamic results are presented in the form of carpet plots. Figure 4 shows the variation of root bending moment (RBM) and drag coefficient (C_D) with respect to the pitch angle for different α and C_L at different span extensions. It is evident from Figure 4 that there are several combinations of α and pitch angles that generate a C_L of 0.5 for various span extensions. For instance, Figure 4a,b shows that, at 0% span extension, the ASAPP wing generates a C_L of 0.5, when operating at $\alpha = 7°$ and 0.5° nose-down pitch angle (of the outboard segment), resulting in a 1.3% reduction in RBM and 1.1% reduction in drag when compared with the baseline wing (non-morphing). It should be noted that all comparisons are made for a fixed C_L of 0.5. This is mainly determined by the weight of the air vehicle and the flight speed, regardless of the span extension. Similarly, Figure 4c,d shows that, at 25% span extension, the ASAPP generates a C_L of 0.5 when operating at $\alpha = 6°$ and a 3.5° nose-down pitch angle, resulting in a 13% drag reduction and 13.5% increase in the RBM relative to the baseline (non-morphing) wing. On the other hand, for the 37.5% and 50% span extension cases, the ASAPP wing can still generate the required lift coefficient; however, the drag and RBM increase significantly for a practical range of α and pitch angle. To illustrate, Table 1 lists the RBM and C_D at different span extensions for the cruise C_L. It is clear from Table 1 that the 37.5% and 50% span extensions increase the RBM significantly (above 20%). For instance, at 37.5% span extension, the RBM increases by 29.81% for $\alpha = 5°$ and 1.9° pitch angle, whilst the drag decreases by 18.8%. Similarly, for 50% span extension, the RBM increases by 29.63% at a 5° angle of attack and 5° pitch angle, whilst the drag decreases by 17.81%. As the encountered loads from 37.5% span extension and 50% span extension conditions significantly increase the RBM (above 20%), for the purpose of this study, the maximum span extension is restrained to 25%. It should be noted that these are only discrete values of span extensions because it is anticipated that the UAV will operate between two states only at 20 m/s. State 1 has a 0% span extension, whilst State 2 has 25% span extension.
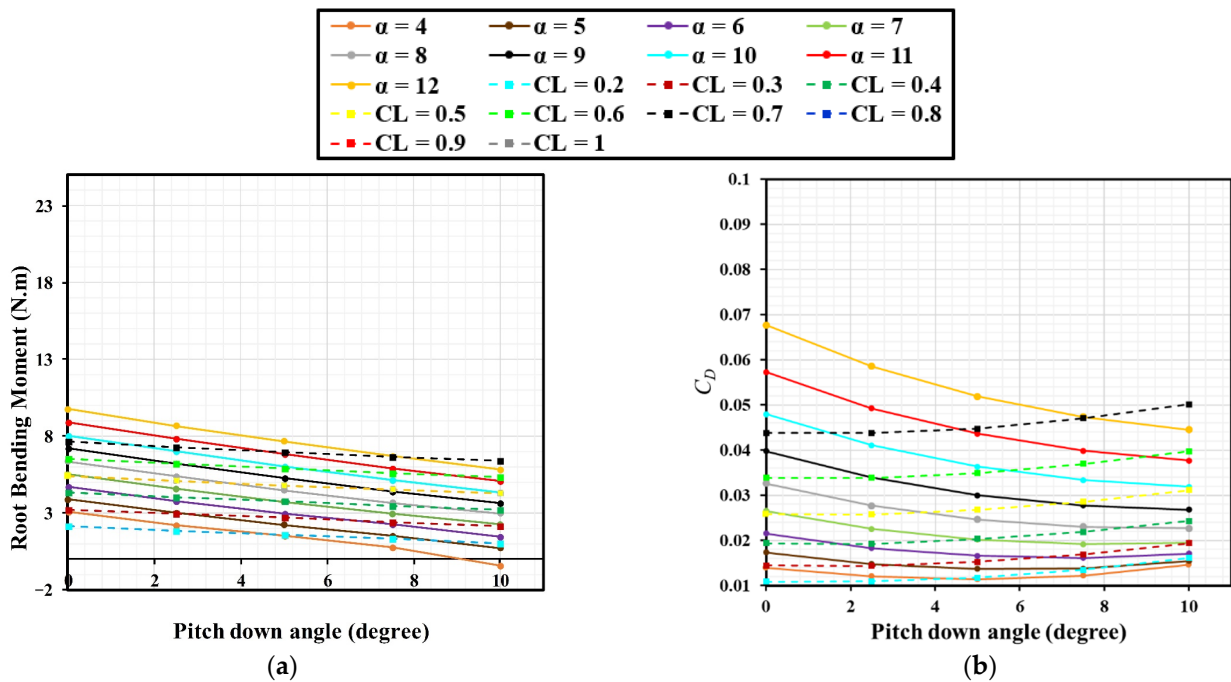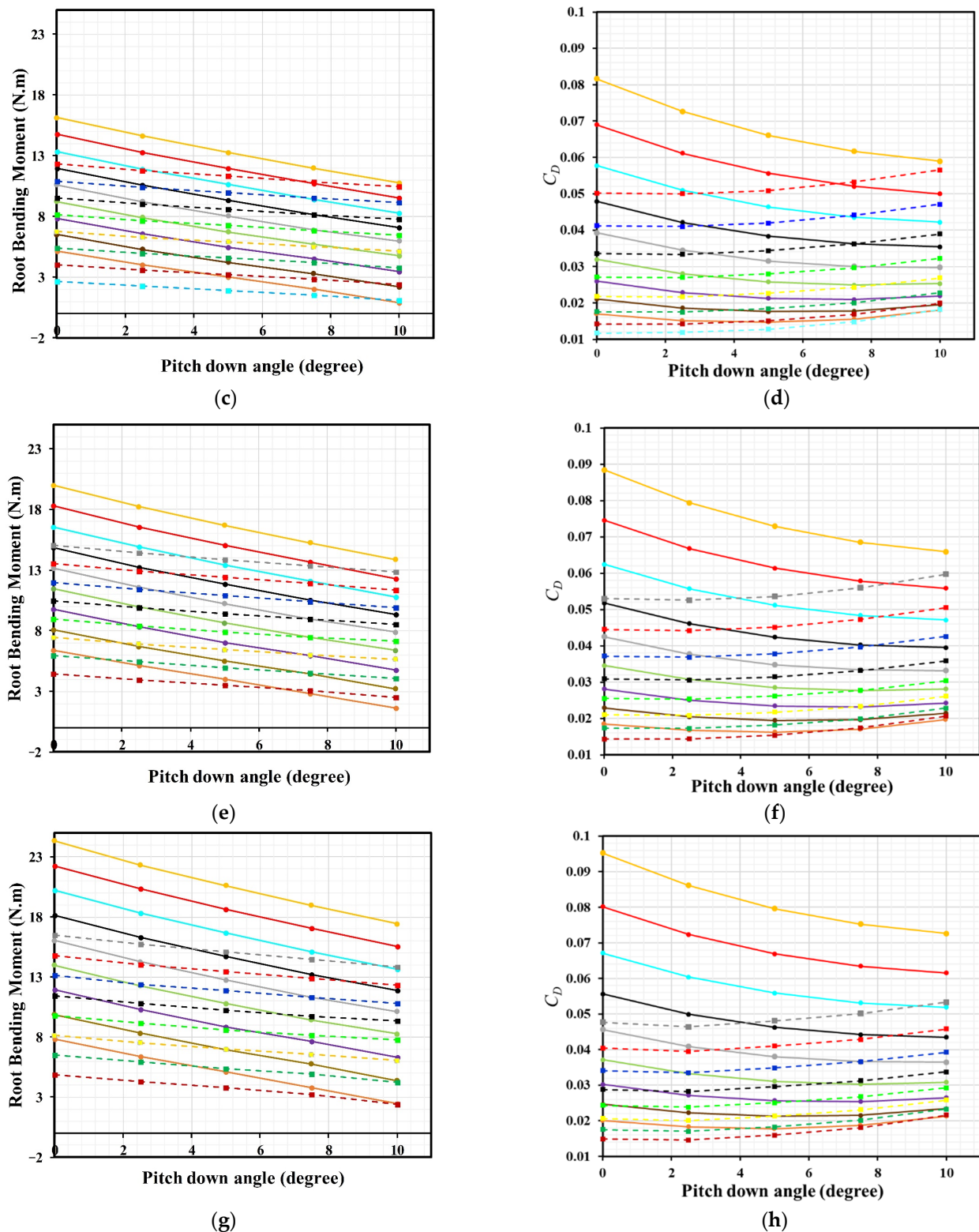

Figure 4. *Cont.*

(**c**)

(**d**)

(**e**)

(**f**)

(**g**)

(**h**)

Figure 4. Variations of RBM and C_D at different span extensions: (**a**) RBM vs. pitch down angle at 0% span extension. (**b**) C_D vs. pitch down angle at 0% span extension. (**c**) RBM vs. pitch down angle at 25% span extension. (**d**) C_D vs. pitch down angle at 25% span extension. (**e**) RBM vs. pitch down angle at 37.5% span extension. (**f**) C_D vs. pitch down angle at 37.5% span extension. (**g**) RBM vs. pitch down angle at 50% span extension. (**h**) C_D vs. pitch down angle at 50% span extension. Reprinted/adapted with permission from Ref. [30]. 2021, American Institute of Aeronautics and Astronautics, Inc.

Table 1. RBM and C_D for different span extensions at C_L = 0.5. Reprinted/adapted with permission from Ref. [30]. 2021, American Institute of Aeronautics and Astronautics, Inc.

Span Extension	α(Degree)	Pitch Angle (Degree)	RBM (Nm)	% Change in RBM	C_D	% Change in C_D
0%	6.88	0	5.4	0.00	0.02596	0.00
	7	0.5	5.33	−1.30	0.02568	−1.10
	8	3.6	4.96	−8.15	0.02641	1.74
	9	7	4.58	−15.19	0.02897	11.60
25%	6	3.5	6.13	13.52	0.02257	−13.06
	7	8.2	5.41	0.19	0.02501	−3.66
37.50%	5	1.9	7.01	29.81	0.02109	−18.76
50%	5	5	7	29.63	0.02134	−17.81

4. Structural Design and Sizing

4.1. Torsional Spring

As stressed above, the inboard and outboard wing segments are connected using a torsional spring. It is important to choose a torsional spring stiffness that reduces root bending moment (RBM) and root shear force (RSF) for high loading scenarios, while also keeping pitching angle to an acceptable value and minimizing structural discontinuity at 1-g cruise flight condition. To assist in selecting a suitable torsion stiffness, a simplified aeroelastic model is developed. The model assumes that the inboard segment of the wing is relatively rigid due to the presence of the main spar and rail, minimizing out-of-plane deformation, allowing the outboard segment to be modeled as a 2D airfoil with the ability to rotate as a rigid body. Based on the above criteria, the one degree-of-freedom model is deemed appropriate to study the model dynamics. The unsteady aerodynamic forces are calculated using Theodorsen's model [32], which accounts for amplitude attenuation and phase lag due to flow unsteadiness. The underlying assumptions of Theodorsen's model include the presence of attached flow, a flat plate airfoil, and a flat wake, which are in consonance with the conditions of the developed model, due to selected design constraints, such as restricting motion to small angles, which validates the use of Theodorsen's model for this case. The equation of motion can be expressed as:

$$I\ddot{\theta} + k_\theta\,\theta \ = M_{hinge} \tag{1}$$

where I is the moment of inertia of the outboard segment around the hinge (overlapping spar), θ is the pitch angle (of the outboard segment with respect to the inboard segment), k_θ is the stiffness of the torsional spring, and M_{hinge} is the aerodynamic moment around the hinge, calculated from Theodorsen's theorem, given as:

$$M_{hinge} = \pi\rho b^2 \left[Vb\left(\frac{1}{2} - \hat{a}\right)\dot{\theta} - b^2\left(\frac{1}{2} + \hat{a}^2\right)\ddot{\theta} \ \right] + 2\pi\rho Vb^2\left(\hat{a} + \frac{1}{2}\right)\ V\theta + b\,\dot{\theta}\ \left(\frac{1}{2} - \hat{a}\right)C\,(k) \tag{2}$$

where ρ is the air density, b is half-chord, V is velocity, $\hat{a}$ is normalized pitch axis location (hinge location), k is reduced frequency, and $C\,(k)$ is Theodorsen's transfer function. The first term in the equation is the non-circulatory or inertial term, whereas the second term is the circulatory term, which includes Theodorsen's function $C\,(k)$. Theodorsen's function accounts for the unsteadiness level of the flow. A gust load analysis is carried out using discrete 1-cosine gusts to determine an optimal torsional spring stiffness to limit outboard spring pitching to an acceptable value for the most critical (highest loading) case.

A maximum gust velocity of 2.5 m/s is considered, with a gust gradient (H) of 12.5 times the mean aerodynamic chord, similar to the work of Gavrilovic et al. [32], as shown in Figure 5. Gust velocity, w_g, is defined as:

$$w_g(t) = \frac{w_{g_{max}}}{2}\left(1 - \cos\left(\frac{\pi V t}{H}\right)\right) \tag{3}$$

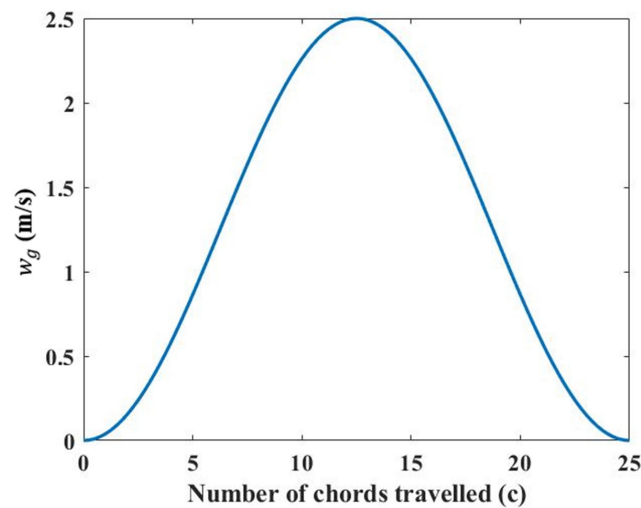where H is the gust gradient and $w_{g_{max}}$ is the maximum vertical gust velocity, chosen to be 2.5 m/s.

Figure 5. Vertical gust velocity profile for 1-cosine gust vs. gust gradient (H) in terms of number of chords travelled.

The developed model is solved using the 4th order Runge Kutta method, for 1-g loading condition, and gust load is applied for the specified gust gradient for varying torsional rigidity, k_θ. The gust is assumed to be encountered during 1-g flight, for both pre-morphing (0%) and 25% span extension cases.

The torsional spring stiffness is selected, which constrains the maximum pitching angle to $-6°$ in the case of design gust gradient, to simulate the worst-case loading scenario, and so a torsional stiffness of 20 Nm/rad is chosen, as shown in Figure 6. The chosen torsional stiffness minimizes structural discontinuity for the encountered gust load while also significantly reducing root loads.
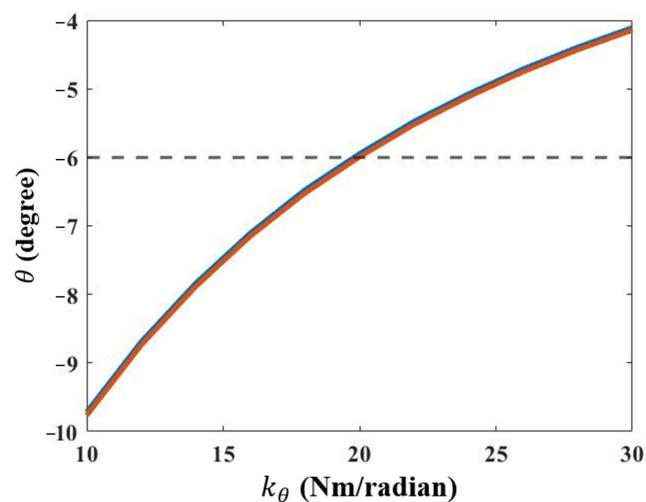
Figure 6. Maximum torsional spring pitching angle vs. torsional spring rigidity. (Solid blue: Pre-morphing (0% span extension), Solid red: Post-morphing (25% span extension), Dashed black: Cutoff value of pitch angle).

To estimate the effectiveness of the passive pitching mechanism, the polymorphing wing is compared with two non-morphing wings (one has a span equal to the baseline wing and one has a span equal to 1.25 the span of the baseline wing). The RBM is estimated using XFLR5 at different flight conditions (1 g (fixed C_L) and discrete gust) for different span extensions with a spring torsional stiffness of 20 Nm/rad. The results are summarized in Table 2. For the gust case, the outboard passive pitch mechanism reduces RBM and RSF by 28.5% and 18.3% for 0% span extension, and 23.7% and 16.5% for 25% span extension, respectively. For the 1-g case, RBM and RSF loads are only slightly reduced by 1.85% and 1.64% for 0% span extension, and 2.81% and 1.99% for 25% span extension, respectively, for the wing equipped with the passive pitching mechanism. It is evident from the results that the outboard passive pitch mechanism can significantly reduce root loads due to gust. For the 1-g loading conditions, the reduction in root loads is not as significant; however, a low pitching angle, θ, ensures minimal structural discontinuity for the steady flight condition.

Table 2. Variation in RBM due to passive pitching mechanism.

Span	α (deg)	θ (deg)	With Passive Pitching				Without Passive Pitching			
			1-g Loading		During Gust		1-g Loading		During Gust	
			RBM (Nm)	RSF (N)	RBM (Nm)	RSF (N)	RBM (Nm)	RSF (N)	RBM (Nm)	RSF (N)
0% span	6.93	−0.26	5.42	18.3	9.04	32.3	5.52	18.6	11.62	38.2
25% span (constant C_L)	6.09	−0.4	7.83	21.1	14.56	40.7	8.05	21.52	18.01	47.4

4.2. Spars

The ASAPP wing must be capable of withstanding the ultimate aerodynamic loads and actuation loads (to overcome skin stiffness). Femap with NX Nastran is used to size the spars. The spars are modeled using beam elements (CBEAM) with the properties of aluminum, and a factor of safety (FOS) of 1.5 is considered. The aerodynamic loads acting on the spars are taken from XFLR5 for the 1-g and 2-g loading scenarios. The aerodynamic loads associated with the 25% span extension condition with a small pitch down angle of 0.4° are applied on the spars as they will contribute more to loading than from 0% span extension, as shown in Table 2. The connecting ribs between the main spar and the overlapping spars are modeled using massless rigid body elements in Femap and are connected to the spars using rigid elements. Aerodynamic loads from XFLR5 are extracted and converted to nodal forces and applied on nodes at the aerodynamic center (at 25% of the chord). The actuation force is applied at the tip of the main spar in the root direction to simulate the reaction force from the latex skin, as shown in Figure 7a.
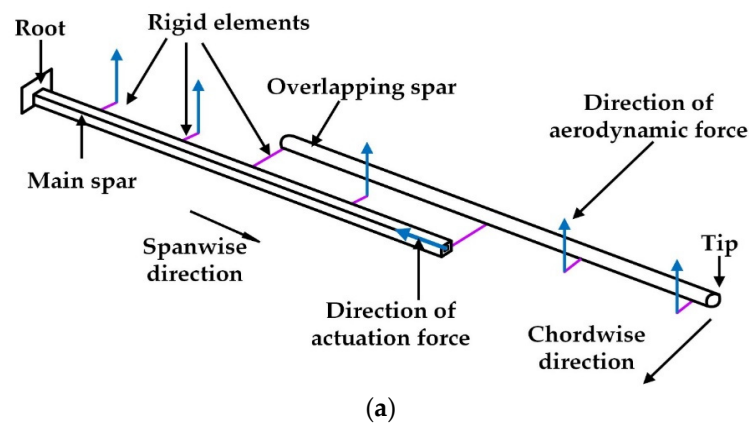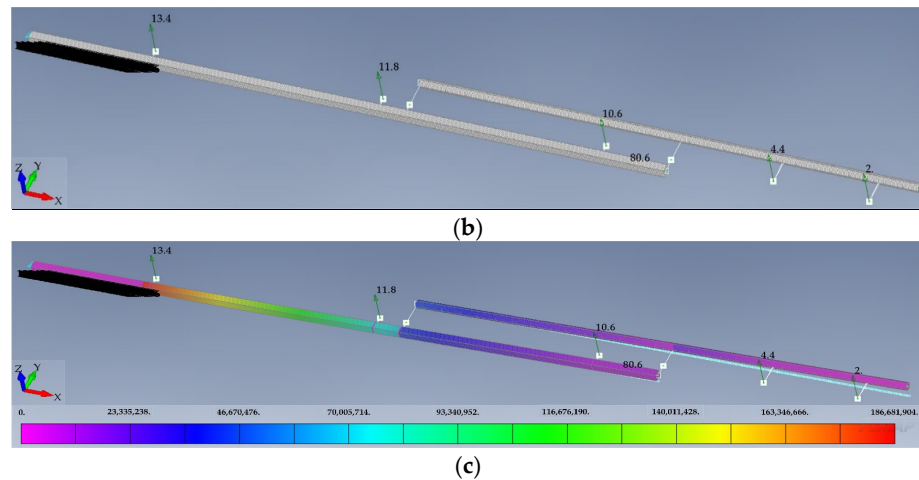

(**a**)

Figure 7. *Cont.*

Figure 7. FEM models of main and overlapping spars: (**a**) Schematic of spar analysis. (**b**) Spars before deformations. (**c**) Spars after deformations (shows combined stresses in Pascal).

Two objectives are set when sizing the spars. The first objective is to maintain the stress below the ultimate allowable stress under 2-g loading conditions and under actuation force. The second objective is to maintain the wingtip out-of-plane deflection at less than 10% of the wing semi-span under the 1-g loading condition [15]. Figure 7b,c shows the spars before and after applying loads under the 2-g condition and actuation force.

The FEM analysis indicates that the main spar with a hollow square cross-section with a depth of 7.5 mm and thickness of 1.25 mm and the overlapping spar of circular cross-section with a diameter of 8 mm and thickness of 1 mm can withstand the applied loads with a FOS of 1.66 (ultimate strength considered is 310 MPa). The rear spar of the outboard segment is subject to very lower loads and therefore a solid circular beam of 6 mm diameter is used.

4.3. Ribs

To size the ribs, a root rib (which is subject to the highest loads) is used. Femap analysis is used to size the rib. Aerodynamic loads are applied as the RSF at the location of the main spar. The RSF is obtained from the spar analysis (Section 4.2) at 2-g loading conditions. The loads from the skin due to actuation are applied as nodal forces in the spanwise direction on the outer surface of the rib. The rib is clamped at the leading-edge and trailing edge sections to simulate the fixing of the rib on the fuselage, as shown in Figure 8a. The rib is modeled using plate elements (CQUAD) with the properties of ABS material. The analysis is carried out with the consideration of a FOS of 1.5. The independent node at the location of the main spar is connected to the rib using massless rigid elements.
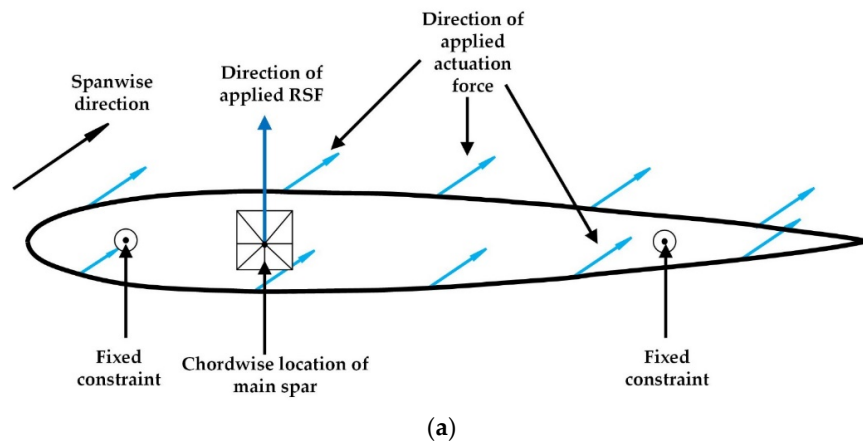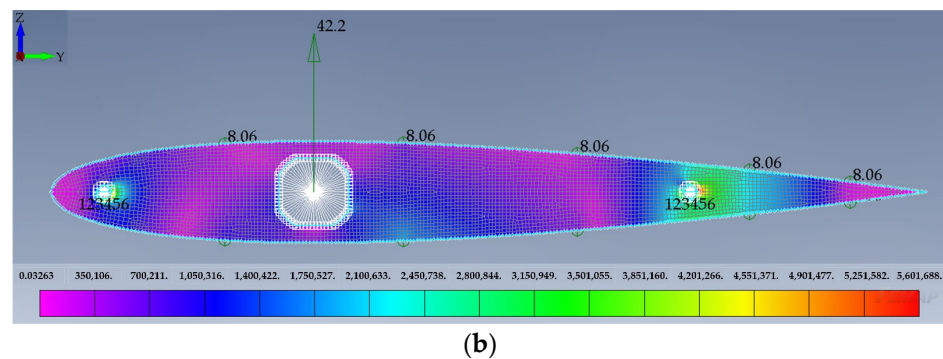

Figure 8. *Cont*.

(**b**)

Figure 8. FEM model of rib: (**a**) Schematic of rib analysis. (**b**) VonMises stress on loaded rib (in Pascal).

The FEM analysis (Figure 8b) indicates that a rib with 10 mm thickness can withstand the applied loads with a FOS of 7.14 (with an ultimate strength of 40 MPa).

4.4. Actuation Force and Skin

The latex sheet, acting as the skin for the inboard segment, has a 0.25 mm thickness. Latex exhibits a nonlinear elastic behavior, making the estimation of the actuation force required to stretch the skin a tedious task. The stress–strain curve for latex obtained from Ref. [15] is used in a nonlinear FEM analysis to predict the required actuation force. Poisson's ratio for the latex sheet is assumed to be 0.49. As the maximum span extension is 25%, larger deformations are not considered.

An FEM model of the inboard segment with three ribs covered by a 0.25 mm latex sheet is used for analysis. A glued connection is used to simulate the attachment between the ribs and the skin. The ribs are made from ABS plastic with Young's modulus of 1.94 GPa and Poisson's ratio of 0.35 [33]. The ribs and skin are modeled using plate (CQUAD) elements. Figure 9 shows the FEM model (using Femap with NX Nastran) of the inboard segment before and after 25% span extension (in meters).

(**a**)　　(**b**)
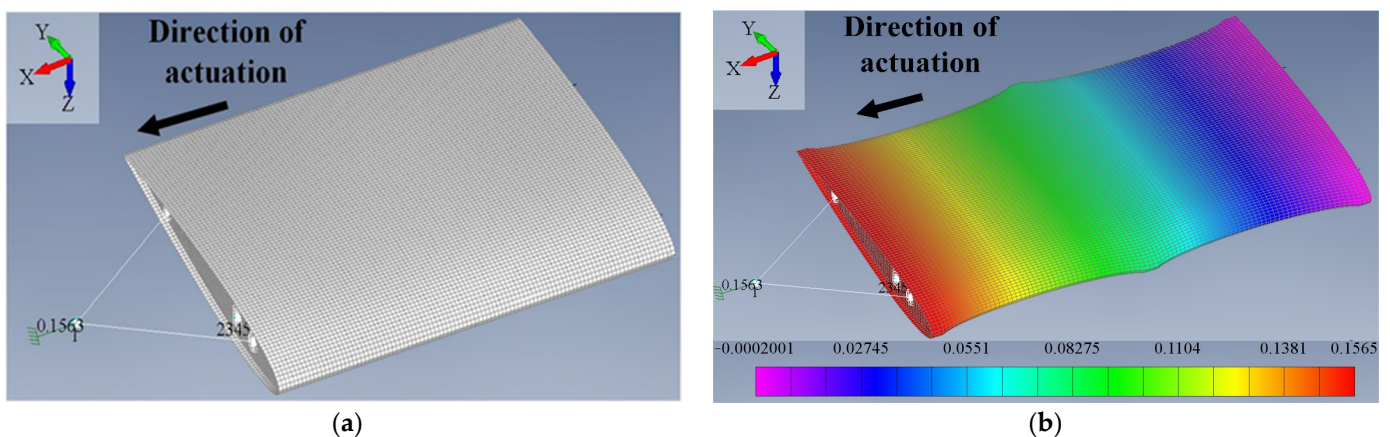
Figure 9. Femap model of inboard segment pre- and post-25% span extension (in meters): (**a**) Before span extension. (**b**) After span extension.

A mesh convergence study is carried out to ensure the accuracy of the FEM analysis. The study is conducted by varying the quadrilateral-type mesh (CQUAD) size from 0.009 m to 0.002 m to estimate the actuation force required for a 25% span extension. It can be seen from Figure 10 that mesh convergence occurs when the mesh size is below 0.003 m.
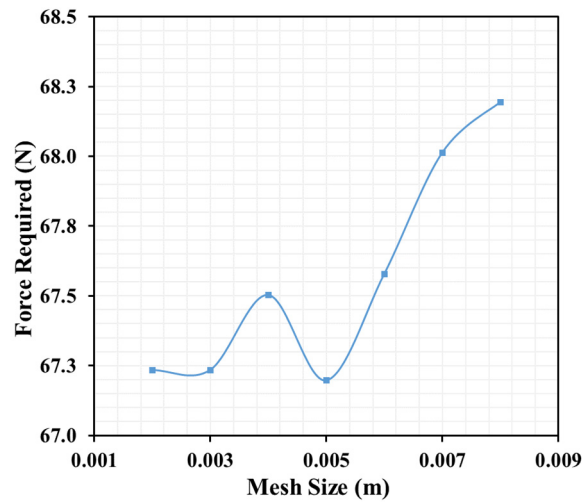
Figure 10. Mesh convergence for actuation force required at 25% span extension in Femap analysis.

It is anticipated that skin pre-tensioning is required to minimize out-of-plane deformation of the skin and eliminate wrinkles. To determine the sensitivity of the actuation force to pre-tensioning and aerodynamics loads, an FEM analysis is carried out. Skin pre-tension is simulated by applying enforced displacement to the inboard tip rib in addition to the span extension. The aerodynamic loads are applied as surface pressure normal to the lower and upper surfaces of the skin.

Figure 11 shows the actuation force required for different span extensions with and without pre-tensioning in the skin and with and without applied aerodynamic pressure. The aerodynamic pressure values are obtained from the XFLR5 analysis. It can be noticed that the required force to extend the span by 25% is 67.2 N at zero pre-tension (equivalent to 52% strain) and 80.6 N at 5% pre-tension (equivalent to 60% strain). Latex skin can undergo very large deformation ($\approx$500% strain) [34] and, therefore, the pre-tensioned skin can easily achieve the maximum span extension without tearing or experiencing other types of failures. Figure 11 clearly shows that skin pre-tensioning can have a significant effect on the actuation force. On the contrary, the presence of aerodynamic pressure on the skin does not have a considerable effect on the actuation force.
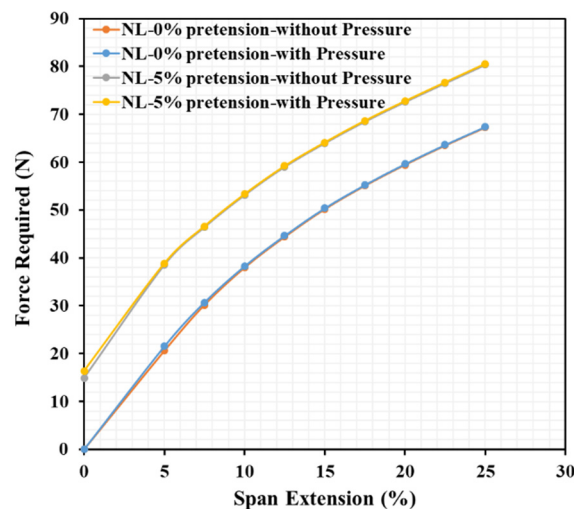
Figure 11. Actuation force for different span extensions at 0% and 5% pre-tensioning.

Figure 12 shows the sensitivity of the skin's out-of-plane deformation to skin pre-tension at different span extensions when subject to aerodynamic loads.
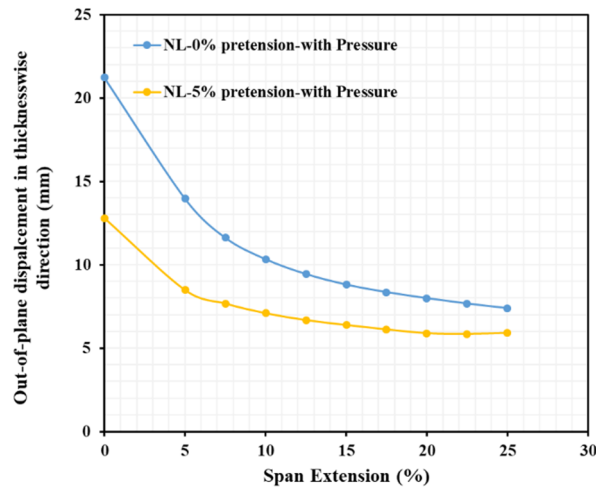
Figure 12. Out-of-plane skin deformation in thicknesswise direction.

From Figure 12, it is clear that a significant reduction in out-of-plane deformation can be achieved by pre-tensioning the skin. For instance, at 0% span extension, 5% pretensioned skin reduced the out-of-plane deformation by 66%. Similarly, at 25% span extension, a 25% reduction in the out-of-plane deformation is observed by 5% pre-tensioning. Therefore, it is decided to apply 5% pre-tension to the skin for the ASAPP wing. However, even with 5% pre-tensioned skin, the out-of-plane deformations are still significant, as shown in Figure 12, which might have a negative effect on the aerodynamic performance of the wing. To reduce the out-of-plane deformation, an FEM analysis is carried out to study the influence of adding more ribs and riblets (as shown in Figure 13).
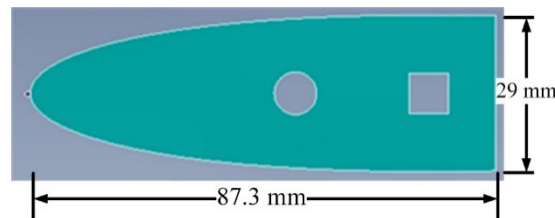
Figure 13. The riblet in Femap.

Three different FEM models of the inboard segment are considered. The first model has three ribs to support the skin, the second has three ribs and two riblets, whilst the third has five ribs. Figure 14 shows the actuation force required for the three FEM models.
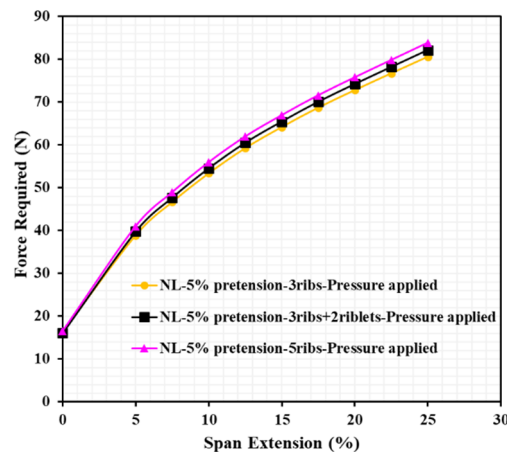
Figure 14. Actuation force for different geometric models.

It can be seen from Figure 14 that adding riblets and ribs slightly increases the actuation force required. This is due to the restriction of the skin at the attached surfaces (where it is glued to). Figure 15 shows the out-of-plane deformations in chordwise and thicknesswise directions for the three models.
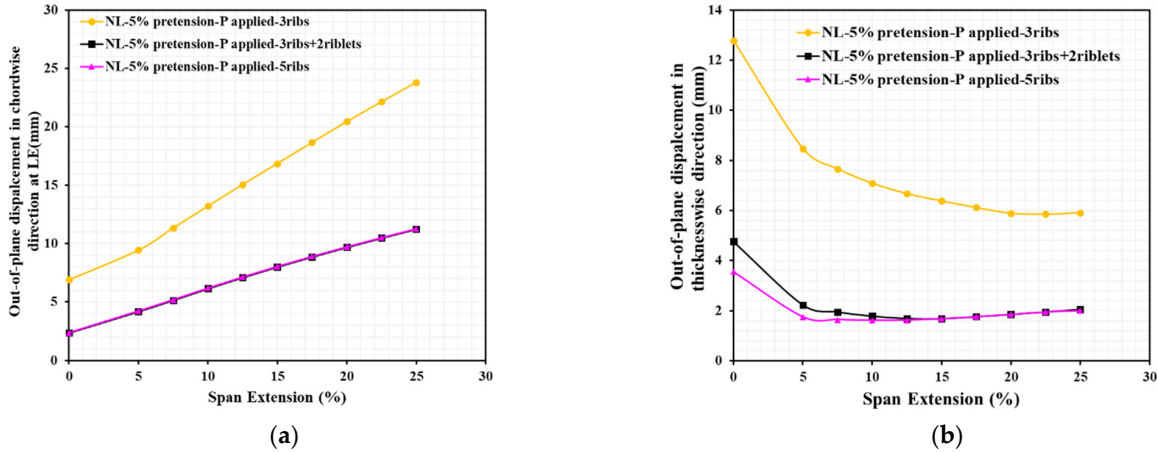

(a)

(b)

Figure 15. Out-of-plane skin deformation for different models (**a**) Out-of-plane deformation in chordwise direction. (**b**) Out-of-plane deformation in thicknesswise direction.

Figure 15 shows that adding riblets and/or ribs reduces the out-of-plane deformation in both chordwise and thicknesswise directions significantly. In addition, the deformation after adding the riblets or additional ribs is the same for chordwise out-of-plane deformation, as shown in Figure 15a. Similar trend exists for the out-of-plane deformation in the thicknesswise direction beyond 10% span extension. It is clear from Figure 15 that after adding the riblets, at maximum span extension with pre-tensioned skin, the chordwise deformation is reduced by 52.8% and the thicknesswise deformation is reduced by 65.3%.

4.5. Aerodynamics of the Inboard Segment

It is essential to determine the influence of the skin deformations on the aerodynamic efficiency of the inboard segment. Therefore, an aerodynamic analysis is carried out on the inboard segment only. XFLR5 analysis is carried out by considering the deformation in the skin due to the aerodynamic pressure during span extension. However, the full coupling between the aerodynamic loads and the deformation in the skin is not considered. The airfoil coordinates for modeling the wing in XFLR5 are obtained from the FEM model. Three span extensions corresponding to 0%, 12.5%, and 25% with three different conditions (three ribs, three ribs and two riblets, and five ribs) are considered. Figure 16 shows the wing segment models in XFLR5 with a 25% span extension. Figure 17 presents the aerodynamic results from the three conditions.
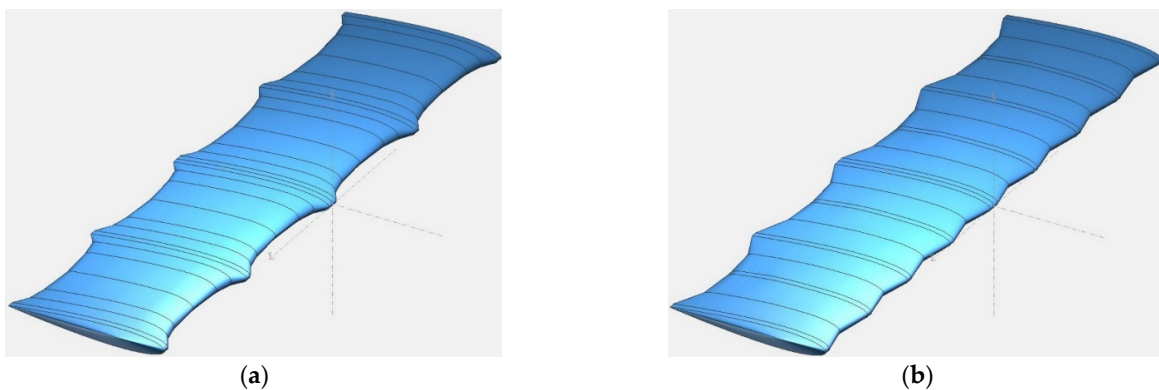

(a)

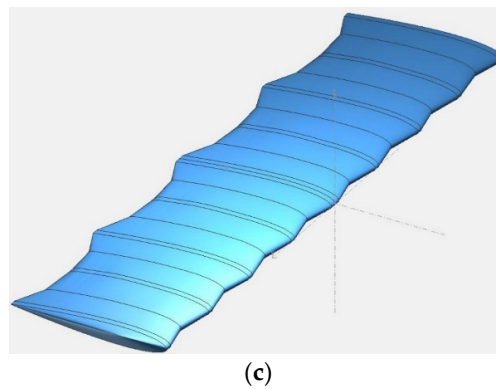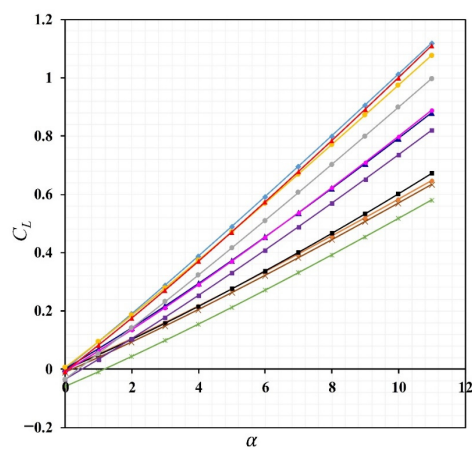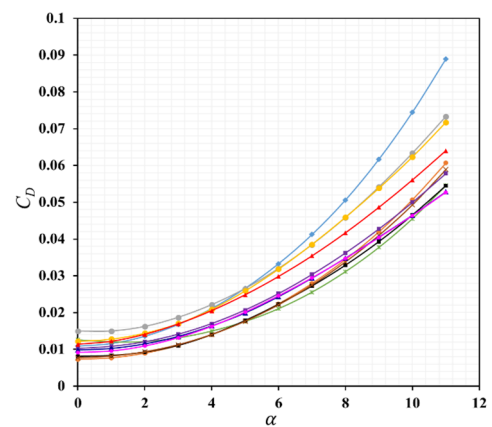**(b)**

Figure 16. *Cont.*

(**c**)

Figure 16. XFLR5 models for 25% span extension with three different geometric conditions. (**a**) With three ribs. (**b**) With three ribs and two riblets. (**c**) With five ribs.
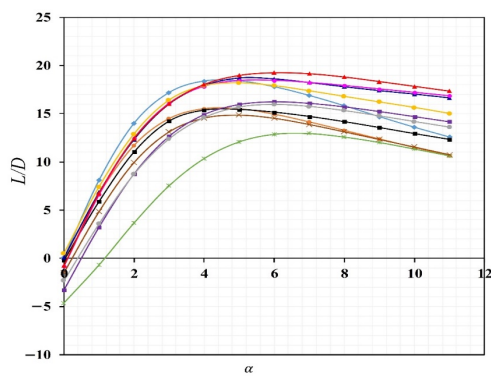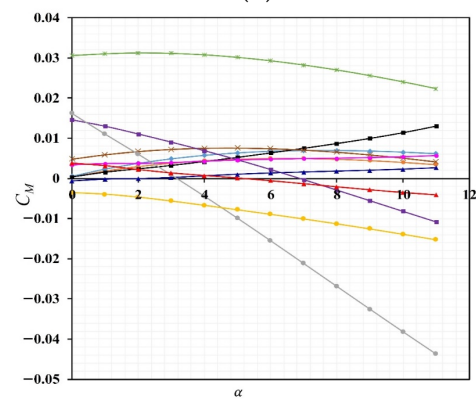

Figure 17. Variations of C_L, C_D, L/D, and C_M with α: (**a**) C_L vs. α. (**b**) C_D vs. α. (**c**) L/D vs. α. (**d**) C_M vs. α.

The coefficient of lift, C_L, for the ASAPP wing segment at 0% span extension with three ribs and two riblets is higher than that with only three ribs or five ribs, as shown in Figure 17a. Additionally, the curve matches with the baseline rigid wing segment below $\alpha = 8°$. For 12.5% span extension, the wing segment with three ribs and two riblets has the same lift curve slope as that of the wing segment with five ribs alone, and that is higher than the wing segment with three ribs alone. This is almost the same for the 25% span extension wing segment as well. In addition, the curves for 25% span extension with flexible skin (three ribs and two riblets, and five ribs) are very close to the curve of the rigid wing segment with the 25% span extension.

The coefficient of drag, C_D, for the ASAPP wing segment at 0% span extension with three ribs and two riblets and with five ribs alone is same as the baseline wing segment below $\alpha = 7°$. Beyond $\alpha = 7°$, C_D is less than that of the baseline wing segment, as shown in Figure 17b. In addition, 0% span extension with three ribs alone reduces C_D for above $\alpha = 5°$ than that of the baseline wing segment. The C_D for 12.5% span extension with five ribs alone, and three ribs and two riblets are lower than that of with three ribs alone. The 25% span extended wing segment with flexible skin (all conditions) has a reduced C_D compared to the rigid wing segment with 25% span extension for above $\alpha = 4°$. The 25% span extension wing segment with three ribs alone has higher C_D than that of the rigid wing segment below $\alpha = 4°$. Below $\alpha = 4°$, the 25% span extension wing segment with three ribs and two riblets, and five ribs alone have almost the same C_D as the rigid wing segment.

From Figure 17c, it is apparent that above $\alpha = 5°$ the 0% span extension wing segment with three ribs and two riblets has higher aerodynamic efficiency than that of other wing segments with 0% span extension and the baseline wing segment. However, irrespective of α, the wing segment with three ribs and two riblets has higher efficiency than that with three ribs alone and five ribs alone. On the other hand, the 12.5% span extended wing segment with three ribs and two riblets and five ribs alone has almost the same efficiency for all α. Above $\alpha = 5°$, those wing segments have higher efficiency than that of the rigid wing segment with the 25% span extension. For 25% span extension, the wing segment with three ribs and two riblets is more efficient than that of the wing segment with five ribs alone at below $\alpha = 4°$, and vice versa for above $\alpha = 4°$. Those are less efficient than the rigid wing segment with a 25% span extension below $\alpha = 4°$. The wing segment with three ribs alone at the 25% span extension is less efficient than that of all other wing segments with 25% span extension. From the aerodynamic efficiency plot, it is clear that, for some cases, wing segments with three ribs and two riblets are more efficient, while other cases have similar results to those with five ribs alone. Therefore, having three ribs and two riblets on the inboard segment of the ASAPP wing is the optimum choice from an aerodynamic point of view.

Figure 17d shows the coefficient of moment, C_M, for different span extensions and geometric conditions. In some cases, C_M varies drastically with α, especially for 12.5% and 25% span extended wing segments with three ribs alone. In addition, for some wing segments, C_M is far beyond zero. It is speculated that these variations in the C_M for the wing segments with flexible skin are due to the change in airfoil shapes in the spanwise directions.

4.6. Fuselage

As mentioned earlier, the fuselage accommodates the span extension actuation system. Moreover, the fuselage must have the structural integrity to withstand the actuation and aerodynamic loads and provide strong support for spars. Therefore, a frame with a 10 mm thick acrylic sheet is used to replicate the fuselage of the UAV. In addition, the fuselage contains acrylic blocks for attaching the linear actuator and the rails, as shown in Figure 18.
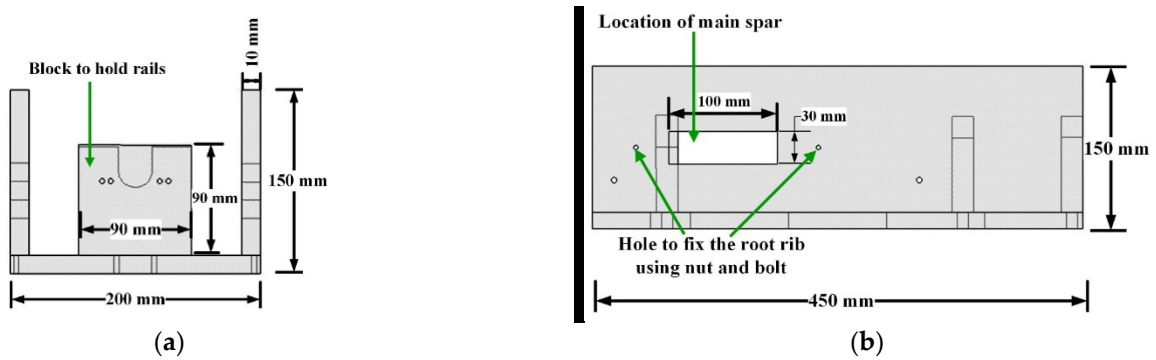
Figure 18. Fuselage frame of the ASAPP wing: (**a**) Front view. (**b**) Side view.

4.7. Linear Actuator

The linear actuator for span extension has a maximum thrust of 600 N, a stroke length of 200 mm, and a weight of 1.04 kg. At the start of span extension, the linear actuator can exert 131.4 N force on each wing, as shown in Figure 19. The main spar of the wing is connected to the hinge block by means of hinges and levers.
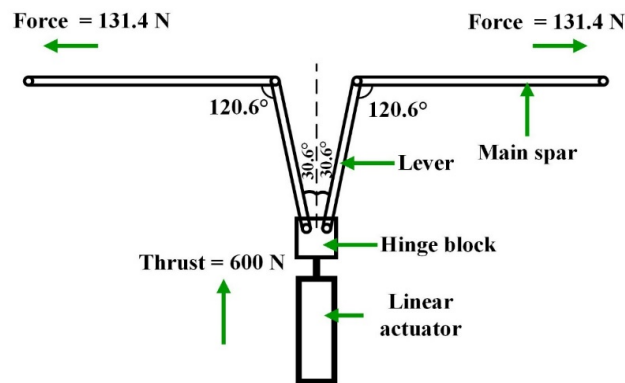

Figure 19. Layout of the actuation mechanism.

5. Manufacturing and Testing

A rig that replicates the ASAPP wing and the fuselage, is manufactured and assembled, as shown in Figure 20.
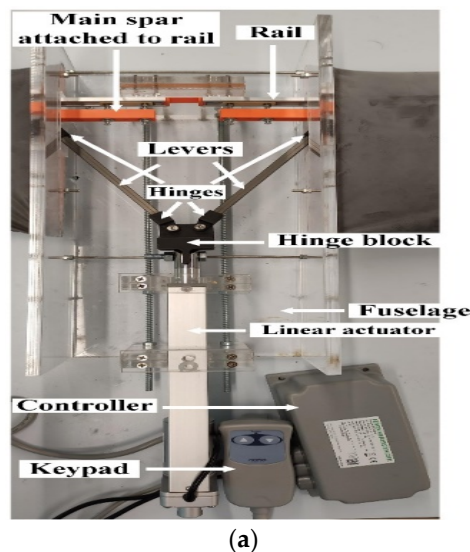

(**a**)

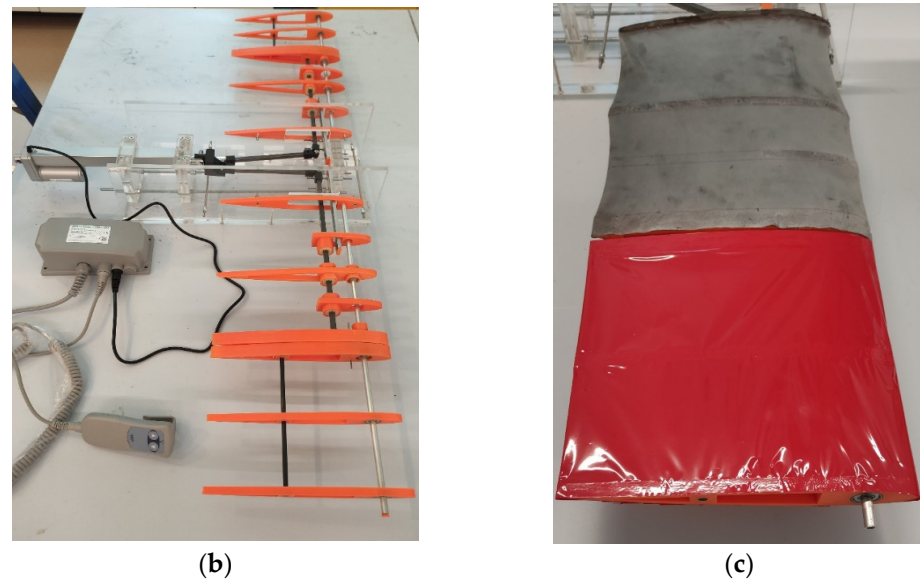**Figure 20.** *Cont.*

Figure 20. Assembled ASAPP wing: (**a**) Actuation system components. (**b**) ASAPP wing without skin. (**c**) Latex and MonoKote film attached.

Figure 21 shows the ASAPP wing before and after span extension and before and after pitch variation.
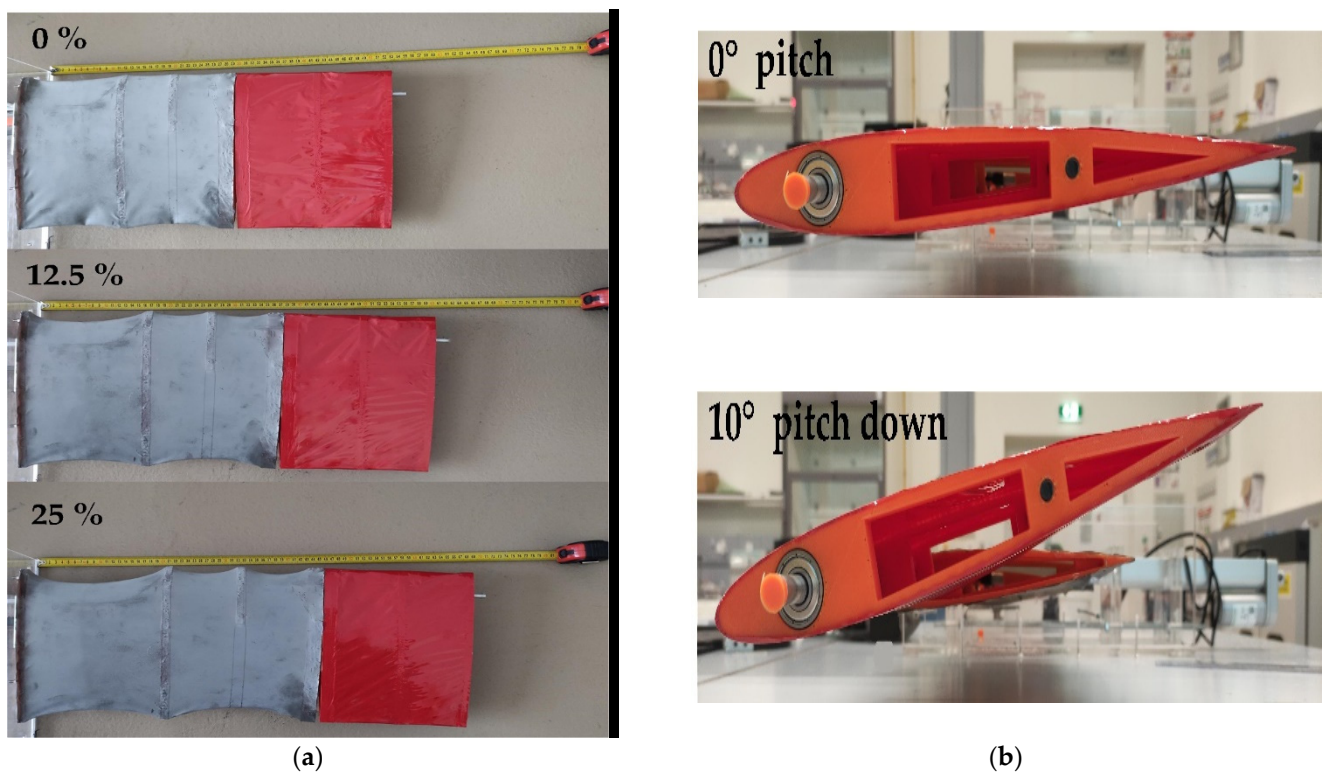

Figure 21. ASAPP wing pre- and post-morphing: (**a**) Before and after span extension. (**b**) Before and after pitching.

Figure 22 shows the close-up of the latex skin at maximum span extension without and with one riblet between two ribs. It is clear that the addition of a riblet between ribs reduces the chordwise Poisson's contraction.

(**a**)   (**b**)

Figure 22. Poisson's contraction in latex skin at 25% span extension: (**a**) Without riblet. (**b**) With riblet.

Then, mechanical testing is carried out to simulate 1-g and 2-g loading scenarios. Static weight is applied at the wingtip, and the deflections are measured. At 0% span extension, 9.5 N is applied at the wingtip to simulate a 1-g loading case and 16.2 N to simulate a 2-g loading case. At 1-g, the tip deflection is 3.8% semi-span and 6.7% semi-span at 2-g. At 25% span extension, 9 N is applied at the wingtip to simulate a 1-g loading scenario and 18.2 N to simulate a 2-g loading scenario. At 1-g loading, the tip deflection is 6.2% semi-span and 8.8% semi-span at 2-g loading.

6. Conclusions and Future Works

The development of a novel polymorphing wing capable of Active Span extension And Passive Pitching (ASAPP) is presented. The ASAPP wing utilized active span extension to enhance the aerodynamic efficiency and passive pitch to alleviate gust and maneuver loads. A linear actuator, located in the fuselage, is used to actuate span extension. The ASAPP wing outperformed the baseline (non-morphing wing) in terms of aerodynamic efficiency without a significant increase in the root bending moment. At cruise, the ASAPP wing with 0% span extension and 0.5° nose-down pitch angle reduces the RBM by 1.3% and drag by 1.1% compared to the baseline (non-morphing), mainly due to passive pitch offloading the tip and shifting the lift distribution inboard. Similarly, at 25% span extension, a 3.5° nose-down pitch angle results in a drag reduction of 13% and an increment in RBM by 13.5% when compared with the baseline wing. The gust analysis shows that a torsional spring with a stiffness of 20 Nm/rad limits the passive pitching angle to a maximum of −6° in the outboard segment, for the highest gust loading. For the highest gust loading case, the outboard passive pitching reduces RBM by 28.5% for 0% span extension, and 23.7% for 25% span extension, respectively. Various methods to reduce the out-of-plane deformation of the flexible skin are investigated, such as skin pre-tension and the addition of riblets. The analysis of the skin shows that, at maximum span extension with pre-tensioned skin, adding riblets between ribs reduces the skin deformation by 52.8% and 65.3% in the chordwise and thicknesswise directions, respectively. An analysis using XFLR5 is carried out to investigate the effect of skin deformation caused by actuation force and aerodynamic pressure in the ASAPP wing at different numbers of ribs and riblets on the aerodynamic results at three span extension conditions: 0%, 12.5%, and 25%. From the aerodynamic point of view, three ribs and two riblets on the inboard segment of the ASAPP wing is an optimum choice as it is superior to three ribs and five ribs at many angles of attacks. In addition, the ASAPP wing with deformed skin exhibits higher aerodynamic efficiency than the rigid wing at α above 5°. Finally, the manufacturing and integration of the ASAPP wing are detailed, followed by mechanical testing to confirm structural integrity. The authors are planning to extend this work by actively controlling the pitch using a flap on the outboard segment.

Abbreviations

Acronyms

ACARE	Advisory Council for Aeronautics Research in Europe
AdAR	Adaptive Aspect Ratio
ASAPP	Active Span morphing And Passive Pitching
EMC	Elastomeric Matrix Composite
FOS	Factor Of Safety
GNATSpar	Gear-driveN Autonomous Twin-Spar
PDMS	Polydimethylsiloxane
PLA	Polylactic Acid
PTWT	Passive Twist WingTip
RBM	Root Bending Moment
RSF	Root Shear Force
SMA	Shape Memory Alloy
VLM	Vortex Lattice Method

Nomenclature

C_L	coefficient of lift
C_D	coefficient of drag
C_M	coefficient of moment
L/D	lift/drag
α	angle of attack
I	moment of inertia about elastic axis
k_θ	stiffness of torsional spring
θ	nose-down pitch angle
M_{hinge}	moment around hinge connecting inboard and outboard wing section
ρ	fluid density
b	half chord
V	velocity
$\hat{a}$	normalized pitch axis location
$C(k)$	Theodorsen's transfer function
k	reduced frequency
w_g	gust load velocity
$w_{g_{max}}$	maximum gust load velocity
H	gust gradient

References

1. Darecki, M.; Edelstenne, C.; Enders, T.; Fernandez, E.; Hartman, P.; Herteman, J.; Kerkloh, M.; King, I.; Ky, P.; Mathieu, M.; et al. *Flightpath 2050: Europe's Vision for Aviation Maintaining Global Leadership and Serving Society's Needs*; Publications Office of the European Union: Luxembourg, 2011.
2. Olivett, A.; Corrao, P.; Karami, M.A. Flow Control and Separation Delay in Morphing Wing Aircraft Using Traveling Wave Actuation. In Proceedings of the ASME 2020 Conference on Smart Materials, Adaptive Structures and Intelligent Systems, Online, 15 September 2020.
3. Olivett, A.; Corrao, P.; Karami, M.A. Flow control and separation delay in morphing wing aircraft using traveling wave actuation. *Smart Mater. Struct.* **2021**, *30*, 025028. [CrossRef]
4. Wang, X.; Zhou, W.; Xun, G.; Wu, Z. Dynamic shape control of piezocomposite-actuated morphing wings with vibration suppression. *J. Intell. Mater. Syst. Struct.* **2018**, *29*, 358–370. [CrossRef]
5. Ajaj, R.M.; Parancheerivilakkathil, M.S.; Amoozgar, M.; Friswell, M.I.; Cantwell, W.J. Recent developments in the aeroelasticity of morphing aircraft. *Prog. Aerosp. Sci.* **2021**, *120*, 100682. [CrossRef]
6. Ouyang, Y.; Gu, Y.; Kou, X.; Yang, Z. Active flutter suppression of wing with morphing flap. *Aerosp. Sci. Technol.* **2021**, *110*, 106457. [CrossRef]
7. Selim, O.; Gowree, E.R.; Lagemann, C.; Talboys, E.; Jagadeesh, C.; Brücker, C. Peregrine Falcon's Dive: Pullout Maneuver and Flight Control Through Wing Morphing. *AIAA J.* **2021**, *59*, 3979–3987. [CrossRef]
8. Rütten, M.; Dölle, B.; Rein, M.; Künemund, J.; Saalfeld, S. Numerical flow investigation of morphing leading edges for the enhancement of maneuverability of unmanned combat air vehicles. In Proceedings of the 30th AIAA Applied Aerodynamics Conference, New Orleans, LA, USA, 25–28 June 2012; p. 3326.
9. Li, D.; Zhao, S.; Da Ronch, A.; Xiang, J.; Drofelnik, J.; Li, Y.; Zhang, L.; Wu, Y.; Kintscher, M.; Monner, H.P. A review of modelling and analysis of morphing wings. *Prog. Aerosp. Sci.* **2018**, *100*, 46–62. [CrossRef]
10. McCormick, B.W. *Aerodynamics, Aeronautics and Flight Mechanics*, 2nd ed.; Wiley: New York, NY, USA, 1995; ISBN 0-471-30899-4.
11. Weisshaar, T.A. *Morphing Aircraft Technology-New Shapes for Aircraft Design*; Purdue University: West Lafayette, IN, USA, 2006.
12. Ajaj, R.M.; Jankee, G.K. The Transformer aircraft: A multimission unmanned aerial vehicle capable of symmetric and asymmetric span morphing. *Aerosp. Sci. Technol.* **2018**, *76*, 512–522. [CrossRef]
13. Samuel, J.B.; Pines, D. Design and testing of a pneumatic telescopic wing for unmanned aerial vehicles. *J. Aircr.* **2007**, *44*, 1088–1099. [CrossRef]
14. Ajaj, R.; Flores, E.S.; Friswell, M.; Allegri, G.; Woods, B.; Isikveren, A.; Dettmer, W. The Zigzag wingbox for a span morphing wing. *Aerosp. Sci. Technol.* **2013**, *28*, 364–375. [CrossRef]
15. Ajaj, R.; Friswell, M.; Bourchak, M.; Harasani, W. Span morphing using the GNATSpar wing. *Aerosp. Sci. Technol.* **2016**, *53*, 38–46. [CrossRef]
16. Vocke, R.D., III; Kothera, C.S.; Woods, B.K.; Wereley, N.M. Development and testing of a span-extending morphing wing. *J. Intell. Mater. Syst. Struct.* **2011**, *22*, 879–890. [CrossRef]
17. Bubert, E.A.; Woods, B.K.; Lee, K.; Kothera, C.S.; Wereley, N. Design and fabrication of a passive 1D morphing aircraft skin. *J. Intell. Mater. Syst. Struct.* **2010**, *21*, 1699–1717. [CrossRef]
18. Woods, B.K.; Friswell, M.I. The Adaptive Aspect Ratio morphing wing: Design concept and low fidelity skin optimization. *Aerosp. Sci. Technol.* **2015**, *42*, 209–217. [CrossRef]
19. Woods, B.K.S.; Friswell, M.I. The Adaptive Aspect Ratio Morphing Wing: Design Concept and Low Fidelity Skin Optimization. In Proceedings of the Smart Materials, Adaptive Structures and Intelligent Systems, Newport, RI, USA, 8–10 September 2014; p. V002T004A027.
20. Bishay, P.L.; Burg, E.; Akinwunmi, A.; Phan, R.; Sepulveda, K. Development of a new span-morphing wing core design. *Designs* **2019**, *3*, 12. [CrossRef]
21. Geva, A.; Abramovich, H.; Arieli, R. Investigation of a Morphing Wing Capable of Airfoil and Span Adjustment Using a Retractable Folding Mechanism. *Aerospace* **2019**, *6*, 85. [CrossRef]
22. Vos, R.; Gürdal, Z.; Abdalla, M. Mechanism for warp-controlled twist of a morphing wing. *J. Aircr.* **2010**, *47*, 450–457. [CrossRef]
23. Rodrigue, H.; Cho, S.; Han, M.-W.; Bhandari, B.; Shim, J.-E.; Ahn, S.-H. Effect of twist morphing wing segment on aerodynamic performance of UAV. *J. Mech. Sci. Technol.* **2016**, *30*, 229–236. [CrossRef]
24. Rodrigue, H.; Bhandari, B.; Han, M.-W.; Ahn, S.-H. A shape memory alloy–based soft morphing actuator capable of pure twisting motion. *J. Intell. Mater. Syst. Struct.* **2015**, *26*, 1071–1078. [CrossRef]
25. Schlup, A.; Bishay, P.; Mclennan, T.; Barajas, C.; Talebian, B.; Thatcher, G.; Flores, R.; Perez-Norwood, J.; Torres, C.; Kibret, K. MataMorph 2: A new experimental UAV with twist-morphing wings and camber-morphing tail stabilizers. In Proceedings of the AIAA Scitech 2021 Forum, Virtual Event, 11–15 & 19–21 January 2021; p. 0584.
26. Rea, F.; Amoroso, F.; Pecora, R.; Moens, F. Exploitation of a multifunctional twistable wing trailing-edge for performance improvement of a turboprop 90-seats regional aircraft. *Aerospace* **2018**, *5*, 122. [CrossRef]
27. Cambier, L.; Heib, S.; Plot, S. The Onera elsA CFD software: Input from research and feedback from industry. *Mech. Ind.* **2013**, *14*, 159–174. [CrossRef]
28. Bishay, P.L.; Aguilar, C. Parametric study of a composite skin for a twist-morphing wing. *Aerospace* **2021**, *8*, 259. [CrossRef]

29. Guo, S.; Los Monteros, D.; Espinosa, J.; Liu, Y. Gust alleviation of a large aircraft with a passive twist wingtip. *Aerospace* **2015**, *2*, 135–154. [CrossRef]

30. Ajaj, R.; Parancheerivilakkathil, M.S.; Amoozgar, M. ASAPP: A polymorphing wing capable of Active Span extension And Passive Pitch. In Proceedings of the AIAA Scitech 2021 Forum, Virtual Event, 11–15 & 19–21 January 2021; p. 0621.

31. Agten, M. *Aerodynamic Analysis of Wings in Airborne Wind Energy Applications: A 3D Potential Flow Solver Extended with a Viscous Correction to Predict Non-Linear Lift and Drag Coefficients at High AoA*; Delft University of Technology: Delft, The Netherlands, 2012.

32. Gavrilovic, N.; Abrantes, G.; Kirsch, B.; Pastor, P.; Benard, E. Passive Gust Energy Extraction of Small UAVs. In Proceedings of the 53nd 3AF International Conference on Applied Aerodynamics, FP45-2018-gavrilovic, Salon-de-Provence, France, 26–28 March 2018.

33. Parancheerivilakkathil, M.S.; Ajaj, R.M.; Khan, K.A. A compliant polymorphing wing for small UAVs. *Chin. J. Aeronaut.* **2020**, *33*, 2575–2588. [CrossRef]

34. Ahmad, D.; Ajaj, R.M. Multiaxial mechanical characterization of latex skin for morphing wing application. *Polym. Test.* **2022**, *106*, 107408. [CrossRef]